Ecological Indicators 167 (2024) 112645

Contents lists available at ScienceDirect

Ecological Indicators

journal homepage: www.elsevier.com/locate/ecolind

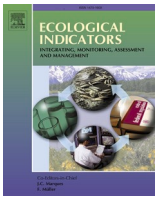

Moderate Red-Edge vegetation index for High-Resolution multispectral remote sensing images in urban areas

Ronghua Li [a], Shiping Ye [b,c,*], Zhican Bai [b,c], Alexander Nedzved [d], Alexander Tuzikov [e]

[a] School of Information Engineering, Huzhou University, Huzhou 313000, PR China
[b] School of Information Science and Technology, Zhejiang Shuren University, Hangzhou 310015, PR China
[c] International Science and Technology Cooperation Base of Zhejiang Province: Remote Sensing Image Processing and Application, Hangzhou 310015, PR China
[d] Belarusian State University, 4, Nezavisimosti Ave, Minsk 220030, Belarus
[e] United Institute of Informatics Problems, National Academy of Sciences of Belarus, 220012 Minsk, Belarus

ARTICLE INFO

Keywords:
Urban green space
UAV remote sensing
Multispectral remote sensing images
Vegetation index
MREVI

ABSTRACT

Urban green space (UGS) monitoring is significant in optimizing urban planning, protecting the ecological environment, and improving residents' quality of life. However, in urban environments, shadow interference and the emergence of new construction materials pose challenges to monitoring green vegetation in high-resolution imagery. This study found that existing vegetation indices (VIs), such as normalized difference vegetation index (NDVI) and enhanced vegetation index (EVI), perform inadequately in extracting vegetation in urban areas, resulting in significant omissions and errors. By conducting in-depth analysis and quantitative experiments on the reflectance of typical urban ground objects, this study developed a new vegetation extraction method, the moderate red-edge vegetation index (MREVI), to enhance the extraction accuracy of UGS vegetation from unmanned aerial vehicle (UAV) high-resolution multispectral remote sensing (RS) images. Experimental results demonstrate that MREVI performs exceptionally well in complex urban environments, significantly suppressing non-vegetation areas, achieving an overall accuracy (OA) of 98.6% and a Kappa coefficient of 0.97. This study supports for urban planning, UGS monitoring, and the evaluation of urban plant carbon sequestration capacity.

1. Introduction

With the acceleration of global urbanization, urban green space (UGS) vegetation coverage continues to decline, resulting in increased ecosystem fragmentation (Chen et al., 2017; Richards and Belcher, 2019; Yang et al., 2018). The expansion of impervious surfaces in cities has triggered a series of severe challenges, including the urban heat island effect, respiratory diseases, and flood hazards, which heighten the potential risks of casualties and economic losses (Ibrahim et al., 2014; Nero, 2017; Wang et al., 2024). UGSs, as a crucial component of urban ecosystems, play a significant role in enhancing urban environmental adaptability and resilience (Chen et al., 2018; Khodadad et al., 2023; Zahoor et al., 2023). They help increase surface water infiltration, mitigate surface runoff from heavy rainfall, and thus reduce the impact of floods on urban infrastructure and residential areas (Kim and Park, 2016; Li et al., 2019; Staccione et al., 2024). This function is particularly critical in highly urbanized areas (Ercolani et al., 2018; Wang et al., 2024). Additionally, green vegetation in UGSs improves air quality by absorbing and filtering pollutants, which reduces the incidence of respiratory diseases (Diener and Mudu, 2021; Fu et al., 2024; Sæbø et al., 2012). Against the backdrop of global climate change, achieving carbon neutrality has become a common goal of the international community. Vegetation and soil in UGSs serve as long-term carbon storage mediums and are key elements in indirectly reducing urban carbon emissions (Zhao et al., 2023; Zhuang et al., 2022). Therefore, protecting and properly utilizing UGSs is essential for mitigating adverse climate events and improving urban environments, and requires the exploration of new technologies to enhance their ecological service functions and support sustainable development.

Satellite remote sensing (RS) technology, with its efficiency, cost-effectiveness, and broad coverage, has become a crucial tool for revealing the spatial distribution and structural characteristics of vegetation (Di et al., 2019; Kopecká et al., 2017; Neyns and Canters, 2022). Many researchers have used satellite imagery for continuous dynamic monitoring of vegetation at various scales. For example, Wang et al. (2021) utilized Landsat TM/ETM+and OLI imagery from 2011 to 2018

* Corresponding author.
E-mail address: ysp@zjsru.edu.cn (S. Ye).

https://doi.org/10.1016/j.ecolind.2024.112645
Received 22 June 2024; Received in revised form 2 September 2024; Accepted 19 September 2024
Available online 24 September 2024

to monitor and assess vegetation recovery in an open-pit coal mine in Dongsheng, Inner Mongolia, China. Lewińska et al. (2020) employed MODIS 8-day reflectance data from 2001 to 2018 to monitor short-term vegetation loss and decadal degradation in the Caucasus eco-region. Beale et al. (2022) quantified the impact of human activities on vegetation cover changes in the lower Bias and Sutlej river basins using Landsat data from 1989 to 2020. However, the spatial resolution limitations of satellite imagery can lead to mixed pixel issues, reducing the accuracy of distinguishing vegetation from other land cover types (Neyns and Canters, 2022; Sathyakumar et al., 2019). Additionally, factors such as weather conditions, revisit intervals, and fixed orbits also constrain the application capabilities of satellite RS (Lyu et al., 2022).

In recent years, unmanned aerial vehicle (UAV) RS technology has gained popularity due to its high resolution, strong timeliness, and flexible data acquisition. UAV RS provides unprecedented insights and data precision, with spatial resolutions ranging from sub-meter to centimeter levels, enhancing the ability to differentiate land cover types in complex landscapes (Behera et al., 2023). Currently, UAV RS has been widely applied in urban mapping, disaster management, precision agriculture, and marine environmental monitoring (Delavarpour et al., 2021; Feng et al., 2015; Hu et al., 2022; Yang et al., 2022). For instance, Feng et al. (2015) effectively differentiated urban vegetation cover types by combining visible light images from UAVs with random forest and texture analysis. Zhang et al. (2021) improved the accuracy of wheat leaf area index and leaf dry matter estimation by integrating vegetation indices (VIs), color indices, and image textures, demonstrating the potential of fixed-wing UAVs in precision agriculture. Song and Park (2020) validated the effectiveness of VIs derived from multispectral UAV imagery for detecting aquatic plants.

Over the past few decades, vegetation index (VI) methods have made significant progress in identifying and extracting vegetation due to their high efficiency and ease of implementation (Gao et al., 2020; Rokni and Musa, 2019; Sotille et al., 2020). Visible, NIR, and shortwave infrared band VIs have been widely used to assess and monitor vegetation health, growth status, and moisture content (Braga et al., 2021; Dong et al., 2019; Gitelson et al., 1996; Liu et al., 2022). Nevertheless, many current UAV-based RS studies rely heavily on RGB images (Guo et al., 2021b; Zhang et al., 2019). For instance, Song et al. (2023) combined high-resolution satellite RS imagery and UAV visible light images, using a newly constructed hue–saturation–value green enhancement vegetation index (HSVGVI) to achieve accurate extraction of desert vegetation and land desertification monitoring in arid regions of northwest China. Yan et al. (2019) proposed a color mixing analysis method based on the HSV color space, which improved the accuracy and efficiency of fractional vegetation cover (FVC) estimation from UAV RGB images. Zhang et al. (2019) introduced a new green–red vegetation index (NGRVI) using UAV visible light images, which outperformed other commonly used visible light VIs in extracting vegetation information in arid and semi-arid areas. RGB VIs, which are primarily based on color information to identify land cover, have limited accuracy in distinguishing features with similar colors (Chen et al., 2024; Xu et al., 2023). To overcome this challenge, researchers are exploring more advanced UAV multispectral and hyperspectral RS technologies to more accurately differentiate and identify various types of vegetation and land cover. Wang et al. (2022a) estimated turfgrass greenness using UAV-mounted multispectral and RGB sensors, indicating that multispectral imagery is more advantageous in capturing non-green vegetation. Sun et al. (2021) proposed a new hyperspectral image-based vegetation index (HSVI), which significantly improved the accuracy of UGS vegetation extraction and addressed the issue of VI saturation.

High-resolution UAV RS technology holds promise for the precise monitoring of UGS vegetation. However, existing studies are constrained by limitations in spectral, spatial resolution, or the complexity of urban environments, and have not yet achieved high-precision extraction of UGS vegetation (Cheng et al., 2023; Wang et al., 2022b; Yu et al., 2016; Zhou et al., 2014). Shadows are an inevitable component of RS scenarios, and in urban areas with dense high-rise buildings, the impact of shadows becomes more pronounced as the spatial resolution of RS imagery increases (Bi et al., 2024; Luo et al., 2020). Shadows can lead to the loss of image information and affect the recovery of the true information of the original scene, causing errors in subsequent vegetation analysis (Tang et al., 2020). Furthermore, the emergence of new construction materials in urban areas, such as artificial surfaces in sports venues and blue roofs, also poses significant challenges to vegetation extraction techniques (Sun et al., 2021; Herold et al., 2004).

There are currently various VIs, each with its advantages and limitations. For example, the normalized difference vegetation index (NDVI) is the most popular index for vegetation assessment, but this does not mean it is universally effective (Huang et al., 2021; Qi et al., 2023). In the process of mapping UGS vegetation, this study found that VIs like NDVI and the enhanced vegetation index (EVI) often misidentify or miss UGS vegetation in high-resolution multispectral imagery from UAVs. This issue is particularly common in areas with shadows, vegetation under shadows, waterproofed roofs, and tennis court surfaces, affecting the accuracy of vegetation information. Therefore, the objectives of this study are: 1) to analyze the spectral reflectance characteristics of typical features in complex urban scenes; 2) to develop a VI suitable for high-resolution multispectral UAV imagery in urban areas; and 3) to compare the newly developed index with several published VIs in terms of vegetation information extraction.

2. Materials and methods

2.1. Study area

Fig. 1 shows the extent of the Gongchenqiao Campus of Zhejiang Shuren University, located in the Gongshu District of Hangzhou, Zhejiang Province, China. This campus was selected as the target area for this study due to its diverse land cover types. The vegetation areas within the campus include trees, shrubs, and lawns, while non-vegetation areas encompass buildings, roads, water bodies, and various sports facilities. The campus buildings are mainly concentrated in the central and western regions, including teaching buildings, libraries, dormitories, and administrative offices, with reasonable spacing between structures.

Hangzhou is located in the subtropical monsoon climate zone, experiences an average annual temperature ranging between 13 °C and 20 °C and an average annual rainfall of about 1400 mm. These climatic conditions, characterized by significant seasonal rainfall, provide ample water resources for vegetation growth. The campus boasts a high vegetation coverage rate, with trees primarily lining the roads and surrounding buildings, offering substantial shading. Shrubs and lawns are widely distributed in open areas and around sports facilities, creating a multi-layered green landscape. The abundant vegetation not only enhances the campus's aesthetic appeal but also contributes to improving air quality and the microclimate, significantly mitigating the urban heat island effect. The diverse land cover types and extensive vegetation cover make the campus an excellent study subject and experimental area for this research.

2.2. UAV multispectral image acquisition and preprocessing

The DJI Matrice 300 RTK UAV was used for data collection in this study. The UAV is equipped with an RTK module to ensure high-precision positioning. The MicaSense RedEdge MX camera was employed for high-resolution multispectral image acquisition, capturing images in five bands: blue, green, red, near-infrared, and red-edge. At a flight altitude of 120 m, the Ground Sampling Distance (GSD) is approximately 8 cm. The central wavelengths and key parameters are shown in Table 1 and Table 2.

The image acquisition was conducted on May 14, 2024, between 9:00 AM and 10:00 AM, under clear weather conditions with consistent

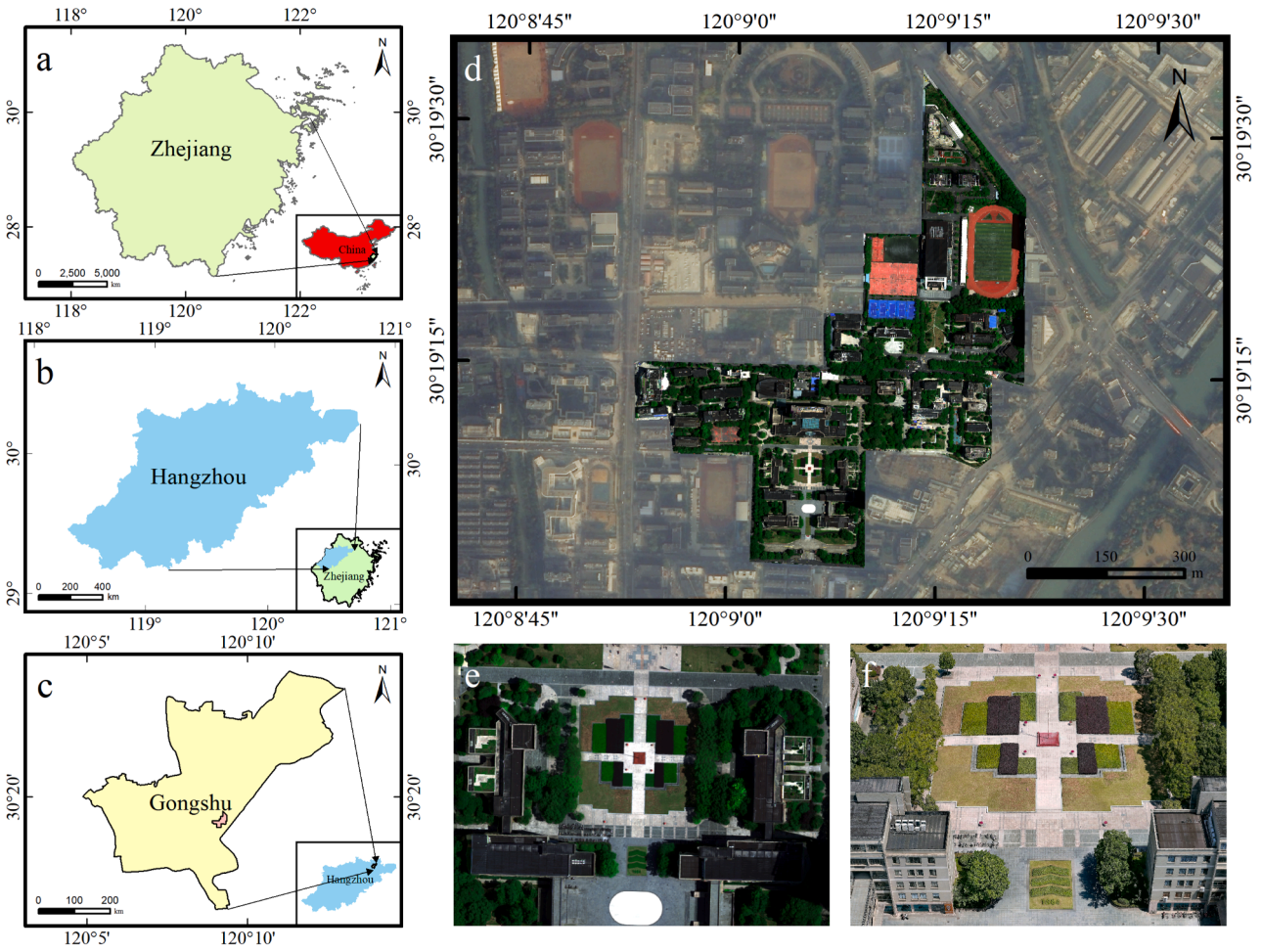

Fig. 1. Map of study area. (a), (b) and (c) show the location map of the study area; (d) digital orthophoto images of UAV in the study area; (e) a cropped orthophoto of Shuren Square in South Campus and (f) its oblique view.

Table 1
Spectral bands of the MicaSense RedEdge MX.

Band Number	Band Name	Center Wavelength (nm)	Bandwidth FWHM (nm)
1	Blue	475	20
2	Green	560	20
3	Red	668	10
4	Near IR	840	40
5	Red Edge	717	10

Table 2
Specifications of the Micasense RedEdge MX.

Items	Contents
Pixel size	3.75 μm
Resolution	1280 × 960 (1.2 MP×5 bands)
Sensor size	4.8 mm × 3.6 mm
Focal length	5.4 mm
Ground sample distance	8 cm per pixel at 120 m AGL
Capture speed	1 capture per second (all bands)

lighting. The flight path was planned using the DJI Pilot 2, and the entire operation was carried out automatically using the flight route mode with equidistant interval photo mode to ensure efficient image capture. The specific flight parameters are listed in Table 3.

This study used the professional UAV image processing software Pix4Dmapper 4.4 to perform orthomosaic generation on the collected

Table 3
Basic parameters of the flight missions.

Sensor	Fly Speed (km/h)	Fly Height (m)	Overlap (%)	Gained images	Aligned images
RedEdge MX	15	115	80	1158	1158

data, generating digital orthophoto maps (DOMs). Simultaneously, radiometric calibration was conducted using images of radiometric calibration panels taken before the flight, along with known standard reflectance information. This produced independent raster files for each spectral band within the study area, with these raster images having identical dimensions. Next, the 'Band Stack' function in ENVI 6.0 was utilized to create a new 5-band TIFF image from these rasters, with an image GSD of 8 cm/px, as shown in Fig. 1(d).

2.3. Spectral reflectance analysis of typical land covers

An analysis of reflectance across different bands was produced to effectively differentiate the spectral characteristics of green vegetation and non-vegetation areas in high-resolution multispectral UAV imagery. In this study, the regions of interest (ROIs) were manually selected on the UAV multispectral orthophoto to analyze the spectral reflectance curves of typical land covers. The considered land cover types encompassed various vegetation types, including trees, shrubs, and lawns, as well as non-vegetation types such as buildings, bare soil, and water

bodies. The mean reflectance for each land cover type across the spectral bands were calculated, resulting in the spectral reflectance mean curves for different typical land cover types in the UAV multispectral imagery, as shown in Fig. 2.

Due to the strong absorption by chlorophyll, vegetation typically has a low reflectance in the visible spectrum, around 10 %, while in the NIR range of 0.7 to 1.3 μm, the reflectance increases to about 50 % (Candiago et al., 2015; Knipling, 1970). The green line in Fig. 2 illustrates the reflectance curve of UGS vegetation, showing the highest reflectance in the NIR band among the five bands, with the NIR and red-edge reflectance significantly greater than that of the visible bands. For three types of typical vegetation—trees, shrubs, and lawns—the curves in Fig. 2 demonstrate similar spectral reflectance characteristics. In contrast, the spectral reflectance curves for non-vegetation categories like roads and buildings show smaller differences in reflectance values between the NIR and visible bands. Generally, the differences in reflectance between the NIR and visible bands allow for the easy distinction between typical vegetation areas and non-vegetation areas through the calculation of VIs (Bhandari et al., 2012; Veraverbeke et al., 2012). However, shadow interference becomes more pronounced for ultra-high-resolution UAV imagery captured at low altitudes due to the dense tall buildings or trees blocking sunlight in urban areas. From the spectral reflectance curves, the reflectance of UGS vegetation under shadow decreases across all spectral bands, particularly in the NIR and red-edge bands (Tang et al., 2020). This reduction significantly weakens the characteristic difference between the NIR and visible bands. Additionally, new construction materials in urban areas, such as the blue surfaces of tennis courts and blue waterproof-coated roofs, exhibit significantly higher reflectance in the NIR band compared to the green and red bands. The reflectance differences among these bands are similar to those of vegetation, which may lead to potential errors in extraction.

Through further analysis of the reflectance curves of various land cover types, it is observed that the red-edge band is effective in distinguishing between vegetation and non-vegetation. Vegetation exhibits lower reflectance in the red band due to chlorophyll's absorption of most red light for photosynthesis (Sims and Gamon, 2002). In the electromagnetic spectrum, the red-edge band is highly sensitive to vegetation and shows a strong correlation with parameters reflecting vegetation growth status (Dong et al., 2019; Guo et al., 2021a). The reflectance of vegetation increases sharply at the boundary between red and NIR, typically within the 670–760 nm range, a phenomenon known as the red-edge effect, which is useful for assessing plant health (Horler et al., 1983; Filella et al., 1994). In contrast, the red-edge band does not show a significant increase for the blue surfaces of tennis courts and blue waterproof-coated roofs, as depicted in Fig. 2.

As part of our methodological approach to establish an effective vegetation index for UAV multispectral imagery, a detailed analysis of the reflectance differences in the five bands for typical land covers was conducted. This analysis included mean values and standard deviations, the results of which are presented in Table 4.

Vegetation shows low reflectance in the red band, with mean reflectance of 2.33 % for trees, 3.33 % for shrubs, 5.57 % for lawns, and 0.54 % for vegetation under shadow cover. In contrast, non-vegetation areas such as roads and buildings have higher reflectance values of 19.24 % and 7.90 %, respectively. Reflectance values in the red-edge band significantly increase for trees, shrubs, lawns, and shadow-covered vegetation, reaching 15.48 %, 24.62 %, 20.35 %, and 2.39 %, respectively. For the blue surfaces of tennis courts and blue waterproof-coated roofs, there is no significant increase in reflectance, and in some cases, a decrease is observed. Reflectance in the NIR band reaches its maximum, with trees, shrubs, and lawns showing higher values than other categories, at 38.41 %, 46.65 %, and 38.28 %, respectively. Due to shadow coverage, the mean NIR reflectance for vegetation drops to 5.37 %. However, the difference between the red-edge and red bands is substantial for vegetation, with mean reflectance increases from the red to red-edge band being 563 % for trees, 639 % for shrubs, 265 % for lawns, and 343 % for shadow-covered vegetation. The red-edge band reflectance values for all vegetation types fall between those of the NIR and red bands, and the differences between red-edge and red, as well as NIR and red-edge bands, are relatively similar. For instance, the difference between the red-edge and red bands for shrubs is 21.29 %, while the difference between NIR and red-edge bands is 22.03 %, yielding a ratio of approximately 1.03. Trees, grasses, and shadow-covered vegetation also show relatively small ratios between these two differences, at 1.74, 1.21, and 1.61, respectively.

Based on the spectral reflectance analysis of typical land cover types, this study identifies the following characteristics that are typical of vegetation but not entirely met by non-vegetation categories: 1) Significant differences in reflectance between the red-edge and red bands; 2) Reflectance in the NIR band is significantly higher than in other

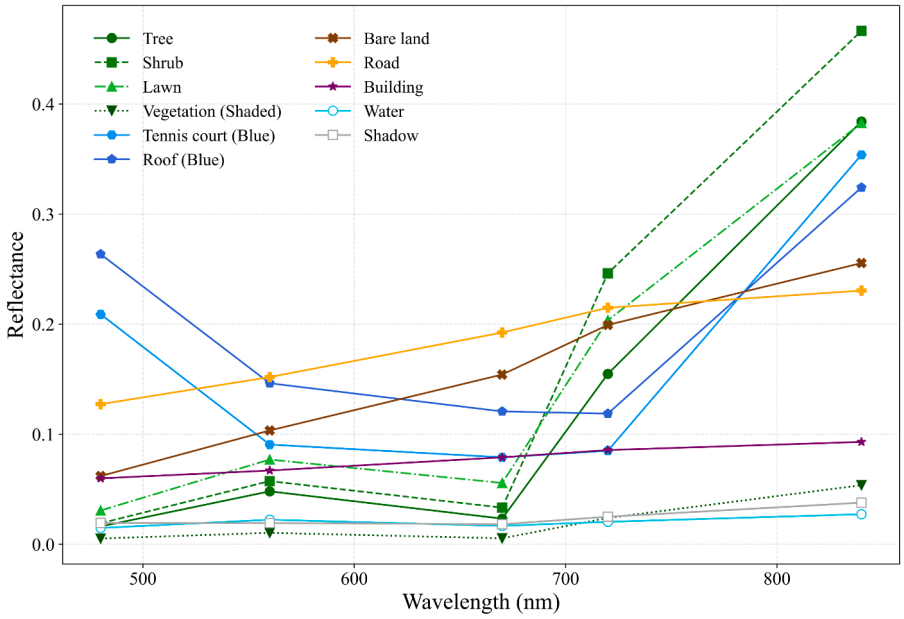

Fig. 2. Reflectance of typical ground objects in different bands.

Table 4
Reflectance in the blue, green, red, red-edge, near-infrared bands of typical objects.

Typical objects	Blue band		Green band		Red band		RE band		NIR band	
	Mean	Sd.	Mean	Sd.	Mean	Sd.	Mean	Sd.	Mean	Sd.
Tree	1.62	0.50	4.81	1.80	2.33	0.82	15.48	5.24	38.41	11.70
Shrub	1.91	0.59	5.74	2.76	3.33	1.62	24.62	3.85	46.65	8.05
Lawn	3.07	0.73	7.70	0.85	5.57	1.87	20.35	2.31	38.28	7.11
Bare land	6.20	0.90	10.34	1.63	15.42	2.02	19.93	2.44	25.55	3.59
Road	12.73	7.05	15.19	8.17	19.24	10.78	21.49	12.06	23.05	12.31
Building	5.99	7.20	6.70	8.13	7.90	10.13	8.56	10.59	9.30	10.38
Water	1.48	0.23	2.23	0.48	1.67	0.36	2.04	0.30	2.73	0.16
Shadow	1.94	1.22	1.93	1.10	1.82	1.06	2.50	1.09	3.78	1.18
Tennis court (Blue)	20.90	3.15	9.06	1.91	7.90	8.00	8.50	0.58	35.39	5.47
Roof (Blue)	26.36	1.76	14.63	4.20	12.07	3.83	11.87	3.43	32.42	3.22
Vegetation (shadow)	0.52	0.12	1.04	0.27	0.54	0.14	2.39	0.56	5.37	1.18

bands; 3) Reflectance in the red-edge band falls between the red and NIR bands, with similar differences observed between red-edge and red, as well as NIR and red-edge bands.

2.4. Construction of the new red-edge vegetation index

Following the analysis presented in Section 2.3, vegetation shows a distinct pattern of reflectance across the red, red-edge, and NIR bands, a pattern that is not observed in non-vegetation categories. Consequently, this study constructs a novel VI utilizing the reflectance characteristics of the red, red-edge, and NIR bands to enhance the accuracy of UGS vegetation extraction.

There is a substantial difference between the mean reflectance of the red-edge and red bands for vegetation. In contrast, non-vegetation types show more minor differences in reflectance between these bands. The normalized difference between the red-edge and red bands has been evaluated and applied in vegetation analysis by some studies (Pu and Landry, 2012; Timmer et al., 2022; Zhu et al., 2017). This feature forms the basis for constructing the new VI in this study, calculated as follows:

$$\mathrm{NDVI}_{\mathrm{rededge}} = \frac{\rho_{\mathrm{RE}} - \rho_{\mathrm{Red}}}{\rho_{\mathrm{RE}} + \rho_{\mathrm{Red}}} \tag{1}$$

Where ρ_{RE} represents the reflectance in the red-edge spectral band and ρ_{Red} represents the reflectance in the red spectral band.

Due to the three-dimensional structure of urban areas, the shadow interference effect is more significant in urban environments than in natural environments. The impact of shadows on vegetation reflectance must be considered (Pu and Landry, 2012). Shadow coverage significantly reduces reflectance in the NIR band, yet vegetation still exhibits a peak in reflectance in this band (Xu et al., 2013). Thus, multiplying by the NIR band can amplify the difference between vegetation, shadowed vegetation, and shadows, mathematically expressed as follows:

$$\frac{\rho_{\mathrm{RE}} - \rho_{\mathrm{Red}}}{\rho_{\mathrm{RE}} + \rho_{\mathrm{Red}}} \times \rho_{\mathrm{NIR}} \tag{2}$$

Where ρ_{NIR} represents the reflectance in the near-infrared spectral band.

Multiplying by the NIR reflectance effectively enhances the index value difference between vegetation and shadowed areas. However, some background regions may have their values incorrectly amplified due to higher reflectance in the NIR band. To further enhance the distinction between vegetation and background, this study applied constraints based on the spectral reflectance curve characteristics of vegetation. This ensures that the red edge band remains at a moderate reflectance level between the NIR and red bands. The mathematical representation is as follows:

$$\frac{max(\rho_{\mathrm{RE}}, \rho_{\mathrm{NIR}}) - max(\rho_{\mathrm{RED}}, \rho_{\mathrm{RE}})}{\rho_{\mathrm{RED}} + \rho_{\mathrm{RE}} + \rho_{\mathrm{NIR}}} \times \frac{min(\rho_{\mathrm{RE}}, \rho_{\mathrm{NIR}}) - min(\rho_{\mathrm{RED}}, \rho_{\mathrm{RE}})}{\rho_{\mathrm{RED}} + \rho_{\mathrm{RE}} + \rho_{\mathrm{NIR}}} \tag{3}$$

In the formula, $max(a, \mathrm{b})$ represents the function that calculates the maximum value between a and b, and $min(a, \mathrm{b})$ represents the function that calculates the minimum value between a and b, where a and b denote the reflectance of any bands.

For vegetation types, the reflectance of the red-edge band is moderate, the corresponding pixel calculations of $max(\rho_{\mathrm{RE}}, \rho_{\mathrm{NIR}}) - max(\rho_{\mathrm{RED}}, \rho_{\mathrm{RE}})$ and $min(\rho_{\mathrm{RE}}, \rho_{\mathrm{NIR}}) - min(\rho_{\mathrm{RED}}, \rho_{\mathrm{RE}})$ will yield relatively moderate values. Consequently, the product of these expressions will be relatively large, effectively preserving the vegetation pixel characteristics. If the red-edge band reflectance is too high or too low, the calculations for the two expressions will produce significantly different values, resulting in a smaller product, and the corresponding land cover pixels will be suppressed as background information. Additionally, Normalization was performed to ensure comparability of results across different land cover pixels.

Thus, the new vegetation index proposed in this study is named the Moderate Red-edge Vegetation Index (MREVI), calculated as follows:

$$MREVI = 100 \times \frac{(max(\rho_{\mathrm{RE}}, \rho_{\mathrm{NIR}}) - max(\rho_{\mathrm{RED}}, \rho_{\mathrm{RE}})) \times (min(\rho_{\mathrm{RE}}, \rho_{\mathrm{NIR}}) - min(\rho_{\mathrm{RED}}, \rho_{\mathrm{RE}}))}{(\rho_{\mathrm{RED}} + \rho_{\mathrm{RE}} + \rho_{\mathrm{NIR}})^2} \times \frac{\rho_{\mathrm{RE}} - \rho_{\mathrm{RED}}}{\rho_{\mathrm{RE}} + \rho_{\mathrm{RED}}} \times \rho_{\mathrm{NIR}} \tag{4}$$

To facilitate comparison and analysis, the results were scaled by a factor of 100 due to the small values obtained from the continuous multiplication of decimal values.

2.5. Binary vegetation image extraction

To extract vegetation from images, it is common practice to set an optimal threshold for vegetation and non-vegetation pixels based on the VI calculated from reflectance RS images, and then binarize the image. When the vegetation index value exceeds the optimal threshold, the pixel is classified as vegetation; otherwise, it is classified as non-vegetation. The mathematical description for extracting vegetation based on the VI threshold is as follows:

$$M(x,y) = \begin{cases} 1, MREVI(x,y) \geq \tau \\ 0, MREVI(x,y) < \tau \end{cases} \tag{5}$$

In the above equation, M represents the binarized vegetation

image, τ is the classification threshold for vegetation and non-vegetation pixels, $M(x,y) = 1$ indicates a vegetation pixel, and $M(x,y) = 0$ indicates a non-vegetation pixel.

In this study, the optimal threshold for the VI was selected based on the principle of maximizing the extraction of vegetation pixels while minimizing the interference from non-vegetation pixels. To achieve this, various thresholds were tested for each VI through multiple trials. The resulting binarized vegetation images were manually compared to determine the optimal segmentation threshold for each VI.

2.6 Reference data and evaluation metrics.

To validate and evaluate the accuracy of the proposed VI in extracting vegetation information, 500 validation points were randomly selected within the study area as reference data. The coordinates of each validation point were randomly generated using a Python program, ensuring no duplicate points were selected. Through manual visual interpretation and field verification, 204 validation points were identified as UGS vegetation types, including trees, shrubs, lawns, and shadow-covered vegetation. The remaining 296 validation points were classified as background types.

The accuracy of the vegetation extraction results was evaluated using metrics related to the error matrix. The error matrix is a tool used to describe classification performance by comparing actual classes with predicted classes, providing a robust evaluation of the VIs performance in accurately extracting vegetation information within urban areas. Specifically, the following key metrics were calculated:

A. Overall Accuracy (OA).

OA represents the proportion of correctly classified pixels to the total number of pixels, reflecting the overall performance of the VI in extracting vegetation information.

$$\mathrm{OA} = \frac{\sum_{i=1}^{k} C_{ii}}{N} \tag{6}$$

where C_{ii} is the element on the diagonal of the error matrix (i.e., the number of correctly classified pixels), N is the total number of pixels, and k is the number of categories. Since vegetation extraction can be considered a binary classification task, classifying pixels as vegetation or non-vegetation, k is 2 in this study.

B. Producer Accuracy (PA).

PA represents the proportion of pixels that actually belong to a particular class that are correctly predicted as that class, mainly used to measure the sensitivity of the VI.

$$\mathrm{PA_i} = \frac{C_{ii}}{\sum_{j=1}^{k} C_{ij}} \tag{7}$$

where C_{ii} is the number of correct classifications for class i, and $\sum_{j=1}^{k} C_{ij}$ is the total number of reference pixels for class i.

C. User Accuracy (UA).

UA represents the proportion of pixels predicted to belong to a particular class that actually belong to that class, mainly used to measure the accuracy of the VI.

$$\mathrm{UA_i} = \frac{C_{ii}}{\sum_{j=1}^{k} C_{ji}} \tag{8}$$

where $\sum_{j=1}^{k} C_{ji}$ is the total number of pixels classified as class i.

D. Kappa Coefficient.

The Kappa coefficient is used to assess the consistency and reliability of vegetation information extraction accuracy compared to actual conditions, considering the effect of chance agreement on classification accuracy.

$$k = \frac{P_o - P_e}{1 - P_e} \tag{9}$$

where P_o is the observed agreement probability, and P_e is the expected agreement probability.

Table 5
The major vegetation indices compared in this study.

Index	Formulation	Reference
NDVI	$(\rho_{NIR} - \rho_{Red})/(\rho_{NIR} + \rho_{Red})$	Rouse et al. (1974)
EVI	$2.5 \times (\rho_{NIR} - \rho_{Red})/(\rho_{NIR} + 6 \times \rho_{Red} - 7.5 \times \rho_{Blue} + 1)$	Huete et al. (2002)
NDRE	$(\rho_{NIR} - \rho_{RE})/(\rho_{NIR} + \rho_{RE})$	Gitelson and Merzlyak (1994)
$\mathrm{NDVI_{rededge}}$	$(\rho_{RE} - \rho_{Red})/(\rho_{RE} + \rho_{Red})$	Pu and Landry (2012)
SVI	$(\rho_{NIR} - \rho_{Red})/(\rho_{NIR} + \rho_{Red}) \times \rho_{NIR}$	Xu et al. (2013)
MGRVI	$(\rho_{Green}^2 - \rho_{Red}^2)/(\rho_{Green}^2 + \rho_{Red}^2)$	Bendig et al. (2015)

3. Experiments and results

3.1. Published vegetation indices

Many scholars have developed various VIs using the spectral reflectance characteristics of visible and multispectral bands for different scenarios (Gao et al., 2020; Li et al., 2016; Rouse et al., 1974). We selected the currently popular and primary VIs from published works to extract and compare the accuracy of UGS vegetation information. The calculation formulas are detailed in Table 5.

3.2. Vegetation index calculation and analysis

Representative areas with different surface features within the study area were selected for comparison to demonstrate the effectiveness and general applicability of the proposed vegetation index. Fig. 3 shows regions containing various typical land cover types, such as large areas of tree cover (Fig. 3(a), 3(e), 3(f)), scattered shrubs (Fig. 3(a)), areas with wilted grassland (Fig. 3(a), 3(f)), blue tennis courts and red basketball courts (Fig. 3(a)), buildings with various colors and styles (Fig. 3(b), 3(c)), shadows caused by building obstructions (Fig. 3(b), 3(c), 3(e)), dark green pond water (Fig. 3(c)), concrete roads (Fig. 3(d)), red plastic tracks and green artificial turf soccer fields (Fig. 3(d)).

High-resolution multispectral RS images from UAVs in the study area were processed using the VIs listed in Table 5. The results of these expressions were linearly stretched to produce grayscale images of the VIs, as shown in Fig. 3.

Fig. 3 shows that vegetation areas are generally brighter in the grayscale images of each VI, while non-vegetation areas are visibly darker. The brightness levels of different vegetation areas vary, with tree-covered regions being the brightest and shrub and lawn areas having relatively lower brightness. The calculation results demonstrate that all the VIs can effectively highlight vegetation-covered areas. However, it is important to note that existing VIs showed varying confusion under complex scene conditions. In an ideal scenario, the index values for vegetation areas should be higher than those for any non-vegetation areas, resulting in higher brightness in the grayscale images. Nonetheless, in the grayscale images generated from NDVI, EVI, NDRE, SVI, and MGRVI, the blue surface of the tennis court appears brighter than some vegetation areas. Similarly, the blue-coated rooftops showed NDVI, NDRE, SVI, and MGRVI high brightness values. EVI successfully suppressed most of the blue-coated rooftops but still showed abnormally high brightness for boundary areas. NDVI, NDRE, $\mathrm{NDVI_{rededge}}$, and MGRVI show higher brightness in shadowed areas caused by building obstructions, while EVI, SVI, and MREVI display lower brightness in these areas compared to vegetation. EVI and SVI show significantly lower brightness in shadowed vegetation areas compared to well-lit vegetation areas, and even lower than some background areas. For the green artificial turf soccer field, NDRE and MGRVI yielded grayscale values similar to grassland. Except for MGRVI, other VIs had lower grayscale values for water areas than vegetation areas.

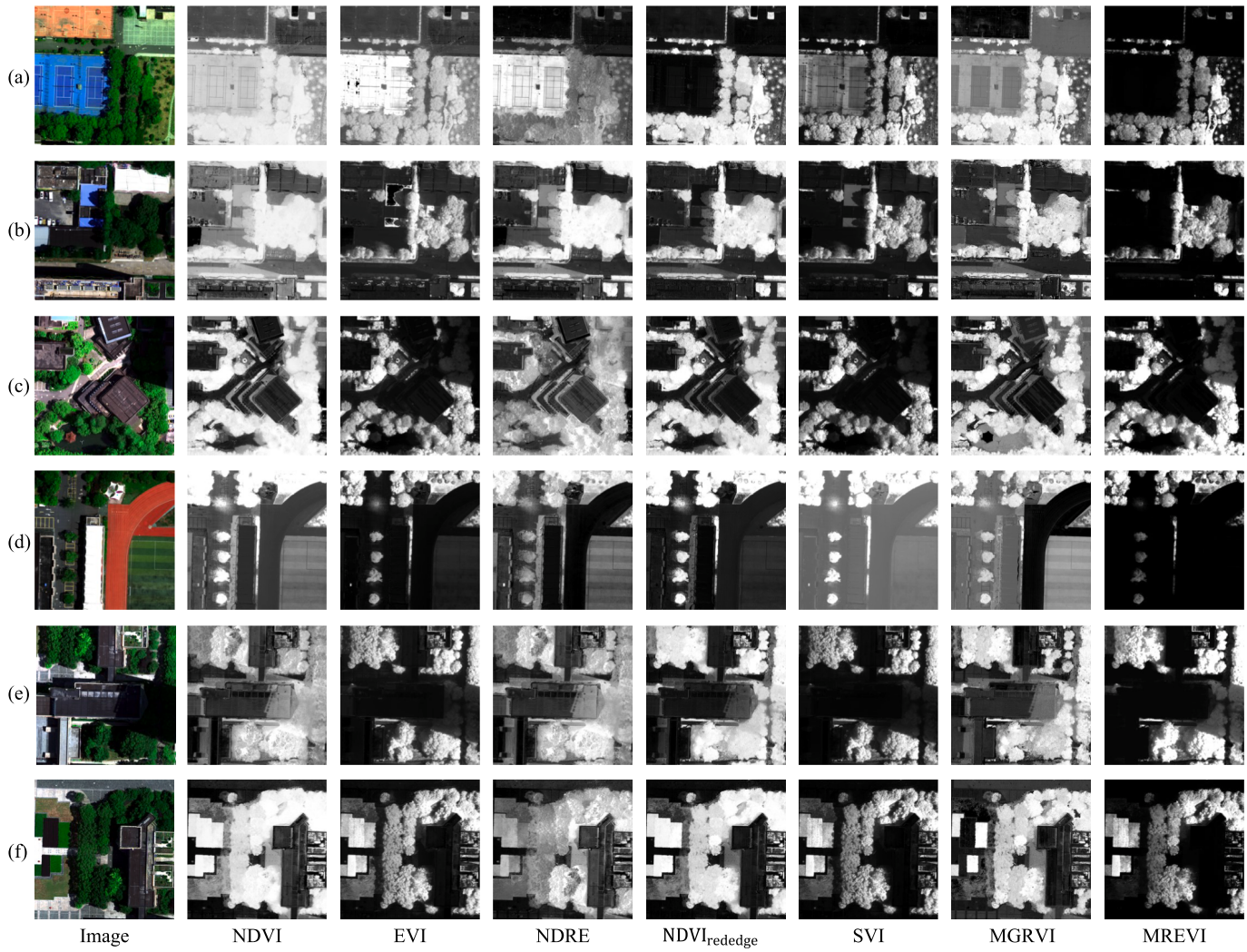

Fig. 3. Grayscale images of vegetation indices.

Table 6
Statistical characteristics of vegetation indices.

Typical objects	NDVI		EVI		NDRE		$NDVI_{rededge}$		SVI		MGRVI		MREVI	
	Mean	Sd.	Mean	Sd.	Mean	Sd.	Mean	Sd.	Mean	Sd.	Mean	Sd.	Mean	Sd.
Tree	0.88	0.03	0.63	0.14	0.42	0.07	0.73	0.04	0.34	0.10	0.60	0.09	2.6865	1.0524
Shrub	0.86	0.04	0.70	0.10	0.30	0.06	0.76	0.05	0.40	0.07	0.35	0.43	3.0076	0.9004
Lawn	0.66	0.15	0.46	0.17	0.26	0.06	0.50	0.16	0.23	0.10	0.09	0.31	1.2170	1.1712
Bare land	0.24	0.05	0.14	0.06	0.02	0.03	0.12	0.02	0.06	0.02	−0.38	0.06	0.0261	0.0178
Road	0.09	0.03	0.06	0.02	0.04	0.02	0.05	0.01	0.02	0.01	−0.21	0.04	0.0014	0.0013
Building	0.12	0.13	0.02	0.06	0.06	0.08	0.06	0.05	0.00	0.01	−0.16	0.14	0.0016	0.0040
Water	0.25	0.10	0.02	0.00	0.14	0.06	0.10	0.05	0.00	0.00	0.28	0.03	0.0033	0.0053
Shadow	0.41	0.15	0.04	0.01	0.23	0.08	0.20	0.08	0.01	0.00	0.07	0.07	0.0184	0.0240
Tennis court (Blue)	0.63	0.02	0.99	0.04	0.60	0.03	0.03	0.01	0.22	0.04	0.11	0.12	0.0091	0.0073
Roof (Blue)	0.46	0.09	−0.05	0.99	0.47	0.08	0.00	0.02	0.15	0.03	0.19	0.04	0.0014	0.0051
Vegetation (shadow)	0.81	0.04	0.11	0.02	0.38	0.04	0.62	0.06	0.04	0.01	0.55	0.14	0.2739	0.1037

The statistical characteristics, including the mean and standard deviation, were calculated for typical land cover types in each vegetation index image using the same ROIs to better compare the reliability of these vegetation index images in extracting vegetation information as shown in Table 6.

In the statistical results of EVI, the vegetation index values for the blue surface of the tennis court showed apparent saturation, and the index values for the blue roofs fluctuated abnormally. In the NDVI and NDRE results, there was overlap and intersection in the grayscale statistical characteristics between shadows, blue-coated roofs, and vegetation types. SVI assigned lower index values to shadow-covered vegetation than some background types. In the MGRVI results, the high standard deviation for shrubs and lawns may cause their index values to overlap with those of background types. According to the statistical

results of $NDVI_{rededge}$ and MREVI, no overlap or intersection was found between the grayscale statistical characteristics of vegetation and non-vegetation types.

3.3. Vegetation information extraction and accuracy evaluation

To further qualitatively and quantitatively evaluate the performance of each VI in extracting UGS vegetation from high-resolution multispectral UAV imagery, a threshold-based classification method was used to generate UGS vegetation images. These images will represent the extracted vegetation information. Through multiple experiments and comparisons, the optimal threshold values for each VI were determined, as listed in Table 7.

In the binarized UGS vegetation images, pixels representing vegetation areas are set to green, while non-vegetation areas (background) are set to black to display the results of vegetation information extraction visually. Consistent with previous analysis, six target areas within the study region, representing various types of land cover, were selected for comparison. These areas include tree cover, shrubs, lawns, artificial turf fields, water bodies, blue-coated rooftops, and shadows. The results of vegetation information extraction using different VIs are shown in Fig. 4.

The binarized images of each VI in Fig. 4 provide a visual reference for evaluating the accuracy of vegetation information extraction. In Fig. 4(a) and 4(b), the vegetation information extraction maps of NDVI, EVI, NDRE, and SVI misclassify the blue surfaces of tennis courts and blue-coated rooftops as vegetation. Except for MGRVI, which failed to exclude water bodies from vegetation types, all other VIs effectively suppressed water body information (see Fig. 4(c)). MGRVI struggled to identify sparsely vegetated grass areas, and failed to recognize the purple shrubs as vegetation (see Fig. 4(f)). NDVI, NDRE, $NDVI_{rededge}$, and MGRVI misclassified some shadow-covered background areas as vegetation (see Fig. 4(b), 4(e), and 4(f)). In Fig. 4(c) and 4(e), In the results of EVI and SVI, there is significant under-extraction of vegetation under shadow coverage. NDRE and MGRVI incorrectly classified parts of the artificial turf soccer field as vegetation (see Fig. 4(e)). The proposed MREVI successfully avoided these issues, providing the most spatially accurate distribution of vegetation pixels compared to UAV RS images.

To quantitatively assess the accuracy of each VI, this study evaluated them using reference data from the experimental area. The error matrix calculated from the extraction results of each VI is shown in Fig. 5. In these matrices, the values on the main diagonal reflect the number of correctly classified instances for each category, while the off-diagonal values indicate errors. NDVI performs best in terms of the number of correct classifications for the vegetation category. In contrast, SVI and NDRE show the highest number of errors in classifying vegetation and non-vegetation categories, respectively. The error matrix for MREVI shows the highest sum of values on the main diagonal, indicating the highest accuracy and the fewest misclassified pixels among all VIs.

The classification accuracy of vegetation and non-vegetation types was easily derived using the error matrix, as shown in Table 8. Compared to other VIs, NDVI has the highest PA for the vegetation category, reaching 99.51 %, while NDRE has the lowest PA for non-vegetation, at only 78.38 %. MREVI achieves the highest UA for vegetation (98.05 %), while SVI has the lowest UA for non-vegetation (84.71 %). For NDVI, EVI, NDRE, SVI, and MGRVI, the Kappa coefficients range from 0.7 to 0.8, indicating a high level of consistency in vegetation information extraction accuracy. The OA of $NDVI_{rededge}$ is 97.00 %, with a Kappa coefficient of 0.93, indicating a high level of precision in vegetation extraction. MREVI shows the best OA at 98.60 %, with a Kappa coefficient of 0.97, demonstrating the superior accuracy of the proposed VI. Overall, MREVI outperforms all other VIs, followed by $NDVI_{rededge}$. NDVI and EVI also show good accuracy. While NDVI, $NDVI_{rededge}$, EVI, and MGRVI perform well on some indicators, their OA and Kappa values are not as high as those of MREVI. In contrast, SVI and NDRE show weaker accuracy in distinguishing between vegetation and non-vegetation.

Table 7
Threshold of vegetation indices.

Vegetation index	Optimal threshold
NDVI	0.4
EVI	0.3
NDRE	0.18
$NDVI_{rededge}$	0.3
SVI	0.15
MGRVI	0.3
MREVI	0.1

4. Discussion

This study introduced a new index, MREVI, and validated its effectiveness in extracting UGS vegetation from high-resolution multispectral UAV images in urban areas. We found that shadow interference and the presence of new construction materials are major factors complicating vegetation extraction in urban environments. Through a detailed analysis of the spectral reflectance characteristics of typical land cover in the study area, it was observed that vegetation exhibits significant variation in reflectance across the red, red-edge, and NIR bands, whereas non-vegetation does not meet these criteria. Based on this pattern, MREVI effectively suppresses background areas that do not meet the vegetation spectral reflectance characteristics. The results of vegetation extraction in the experimental area show that MREVI performs exceptionally well in urban areas, significantly addressing the challenges in vegetation information extraction and effectively reducing both over-extraction and under-extraction issues. The OA and Kappa coefficient reach 98.6 % and 0.97, respectively, marking improvements of 1.6 % and 4 % compared to the second-highest accuracy achieved by $NDVI_{rededge}$.

Shadows are often considered noise in RS images as they alter the spectral characteristics of objects and may interfere with the analysis of ground surface (Alavipanah et al., 2022; Wójcik-Długoborska and Bialik, 2020). The reflectance and spectral curve shapes of shadowed vegetation differ from those of vegetation under sunlight, impacting the calculation of VIs (Zhang et al., 2015). Due to a significant decrease in reflectance, EVI and SVI fail to effectively extract vegetation under shadow, resulting in substantial loss of vegetation information and a decrease in accuracy. The spectral characteristics of shadowed areas resemble the variation patterns of vegetation in certain bands, which is a primary cause of confusion for many VIs. NDVI, NDRE, $NDVI_{rededge}$, and MGRVI misclassify shadow pixels as vegetation, increasing extraction errors. Although reflectance decreases, shadowed vegetation still shows a significant peak in the NIR band (Xu et al., 2013). By considering this feature, MREVI enhances the distinction between vegetation, shadowed vegetation, and shadows. Therefore, MREVI effectively mitigates the negative impacts of shadows in high-resolution imagery, accurately extracting vegetation in shadowed regions and suppressing shadows.

On the other hand, the emergence of new materials in urban areas adds complexity to classification scenarios (Herold et al., 2004). In the study area, blue surfaces of tennis courts and roofs have partially affected the performance of existing VIs, leading to errors and omissions in extraction. NDVI, EVI, NDRE, and SVI struggle with this confusion due to reflectance differences in the NIR and red bands that are similar to those of vegetation. By utilizing reflectance characteristics in the red-edge band, MREVI effectively distinguishes these areas from vegetation, as these areas do not show a significant increase in reflectance in the red-edge band.

The quality of RS images may be affected by factors such as terrain complexity, lighting conditions, sensor quality issues, and radiation calibration accuracy, potentially resulting in anomalous spectral information (Cao et al., 2019). For instance, in certain anomalous conditions, reflectance in the red-edge band may exceed that in the NIR band,

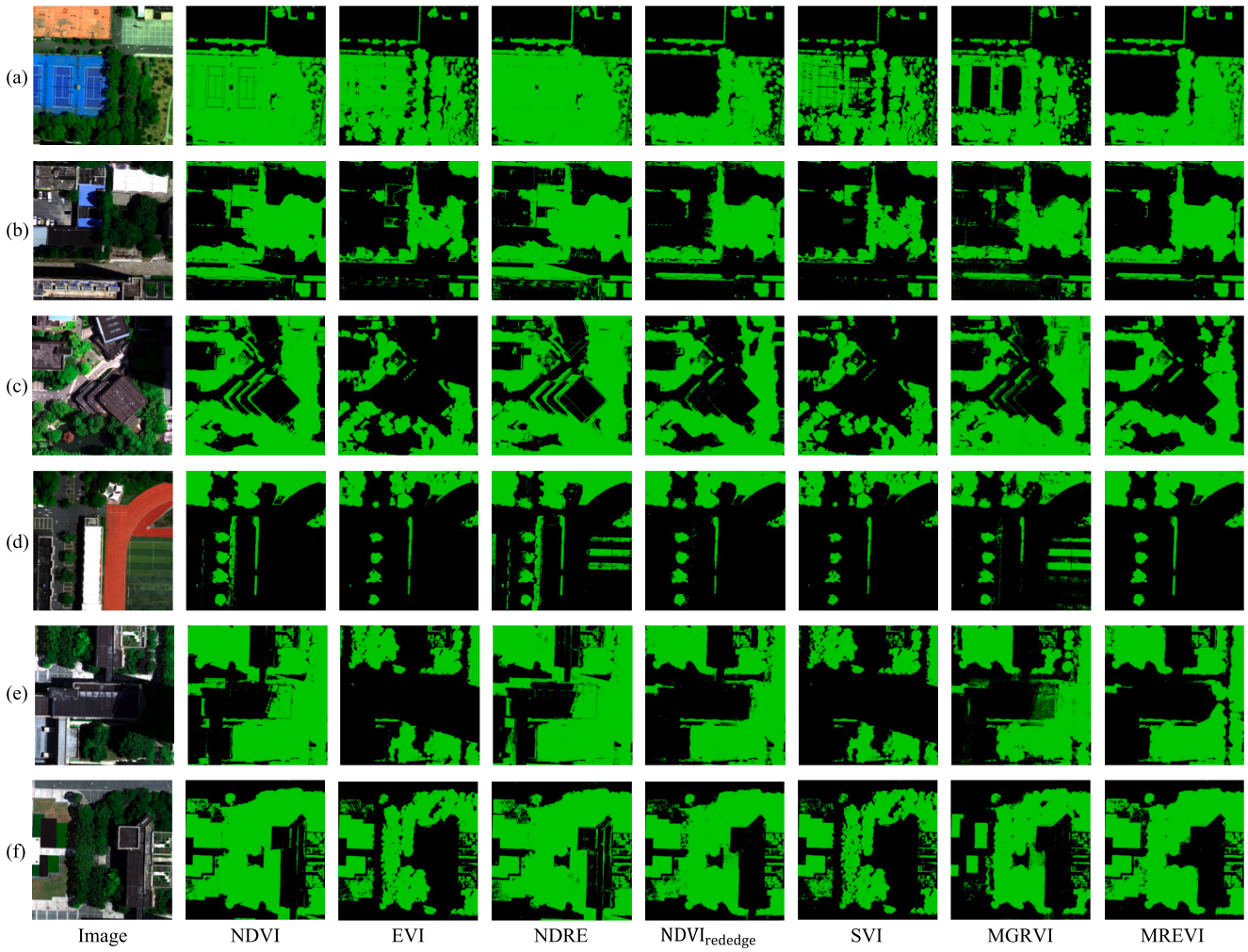

Fig. 4. Extraction results using different vegetation indices.

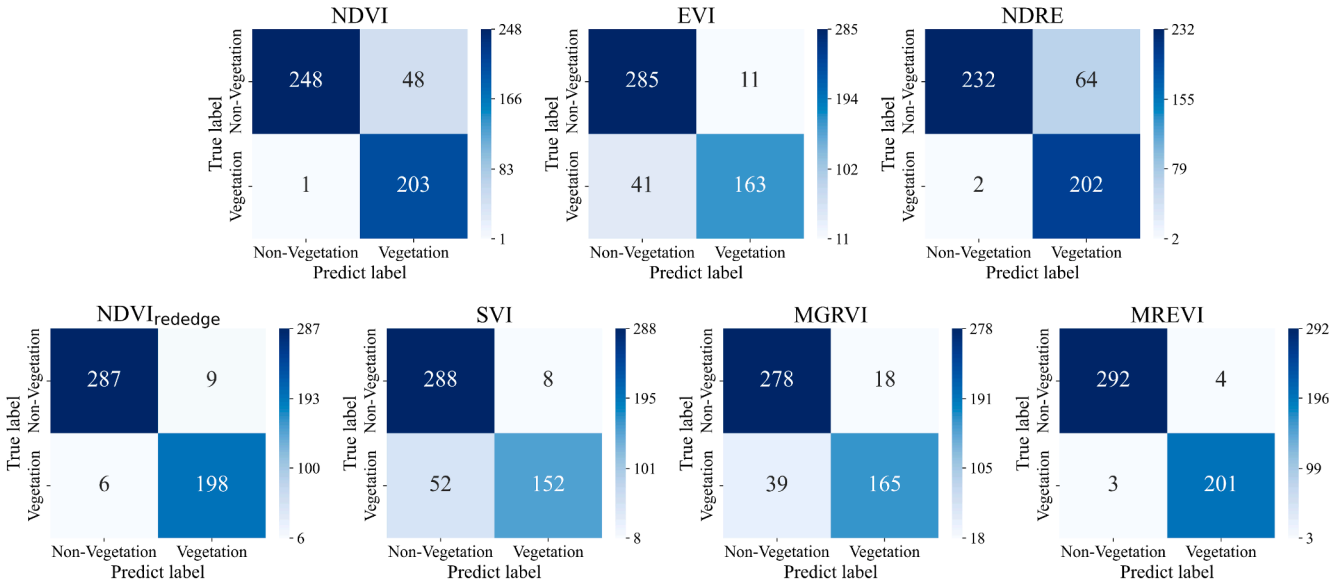

Fig. 5. Error matrix of vegetation index extraction results.

Table 8
Evaluation of vegetation extraction accuracy.

Vegetation index	Producer Accuracy (%)		User Accuracy (%)		Overall accuracy (%)	Kappa
	Vegetation	Non-vegetation	Vegetation	Non-vegetation		
NDVI	99.51	83.78	80.88	99.60	90.20	0.80
EVI	79.90	96.28	93.68	87.42	89.60	0.77
NDRE	99.02	78.38	75.94	99.15	86.80	0.73
$NDVI_{rededge}$	97.06	96.96	95.65	97.95	97.00	0.93
SVI	74.51	97.30	95.00	84.71	88.00	0.74
MGRVI	80.88	93.92	90.16	87.70	88.60	0.76
MREVI	98.53	98.65	98.05	98.98	98.60	0.97

contrary to the spectral characteristics of vegetation. In such cases, MREVI calculates values as 0, effectively eliminating this type of noise interference.

In terms of the completeness and accuracy of vegetation information extraction, $NDVI_{rededge}$ performs well overall but still fails to avoid the impact of shadow interference, which is a major cause of increased extraction errors. NDRE and MGRVI show significant issues with both omission and commission errors. For instance, due to overlapping VI values with grass types, artificial turf fields are identified as vegetation. MGRVI, which is based on visible light bands, performs poorly in extracting vegetation due to limited spectral information. It struggles to identify non-green vegetation, such as purplish shrubs, and produces a substantial amount of noise in the results. In contrast, MREVI achieves the best performance in vegetation extraction within the study area. It excels in identifying wilted lawns, effectively suppresses shadow interference, and shows fewer issues with holes and noise. Additionally, the grayscale images computed from the MREVI vegetation index show different brightness levels for vegetation areas, while non-vegetation types are effectively suppressed, appearing almost black. The grayscale difference between vegetation and non-vegetation areas is clear, with no evident overlap in grayscale statistical characteristics, facilitating the determination of an appropriate threshold for extracting UGS vegetation.

The effectiveness of vegetation extraction is largely determined by the choice of vegetation index; however, the selection of the segmentation threshold is also crucial. In this study, we used a manual approach to select the threshold, which inevitably introduced subjectivity. To improve the objectivity and accuracy of threshold selection, exploring automatic threshold selection methods is worthwhile. Such methods could reduce human bias and potentially improve both the efficiency and accuracy of vegetation extraction (Chen et al., 2022; Dong et al., 2008). Furthermore, the scope of the image data analyzed in this study is limited; thus, the applicability and precision of the newly developed MREVI need broader validation in future research. With technological advancements, many modern multispectral sensors, including Sentinel-2, WorldView-2 satellites, and multispectral cameras mounted on UAVs, now offer red-edge bands, providing greater potential for the application of MREVI (Delegido et al., 2013; Guo et al., 2021a). Therefore, future research should focus on expanding the applicability of MREVI to various environments and sensor data, and explore automatic threshold selection methods to enhance the automation and accuracy of vegetation extraction.

The proposed MREVI significantly enhances the accuracy of vegetation extraction in urban environments and holds broad application potential in supporting decision-making and management across several critical areas of environmental protection. For instance, in UGS management, MREVI can assist city planners in identifying changes in urban FVC, developing more rational greening strategies, and improving the quality of life for urban residents (Cao et al., 2024; Richards and Belcher, 2019). By accurately identifying vegetation cover in cities, researchers can gain deeper insights into the role of vegetation in regulating urban climates and develop corresponding mitigation strategies (Zhou et al., 2023). High-precision vegetation cover data can also help estimate urban vegetation's carbon sequestration capacity more accurately, aiding city managers in assessing the effectiveness of greening measures on carbon emission reduction and providing technical support for low-carbon city initiatives (Qin et al., 2022; Deng et al., 2024). Future research should further explore MREVI's role in broader environmental monitoring and management contexts, offering scientific evidence for urban planning and greening and promoting sustainable urban development.

5. Conclusions

This study developed a novel vegetation index (VI), the moderate red-edge vegetation index (MREVI) suitable for urban areas. It is designed to handle urban complexity and improve the accuracy of extracting urban green space (UGS) vegetation from unmanned aerial vehicle (UAV) high-resolution multispectral remote sensing (RS) images. The study also compared the accuracy of vegetation extraction between the newly developed MREVI and several published VIs. The conclusions are as follows:

(1) Published VIs are subject to interference from shadows and new urban materials, leading to varying degrees of misclassification and omission, which limits the accuracy of vegetation extraction.
(2) The experiments in this study show that MREVI performs exceptionally well in urban areas. The inclusion of the red-edge band aids in identifying vegetation and significantly enhances the suppression of background interference.
(3) The spatial distribution of vegetation pixels extracted by MREVI is highly consistent with UAV RS images. The overall accuracy (OA) and kappa coefficient of vegetation information extraction reach 98.6 % and 0.97, respectively.

In summary, MREVI shows great potential in improving the accuracy of UGS vegetation extraction; however, there are some limitations in this study. This research is primarily based on high-resolution remote sensing data from a specific region, and the results may be constrained by the spatial and temporal resolution of the data, spectral characteristics, and sensor performance. Therefore, the applicability of MREVI in different regions and diverse environments needs further validation. Future studies should apply MREVI to various environments and sensor data to assess its qualitative and quantitative accuracy in UGS vegetation extraction under different climates, seasons, and land cover types. Moreover, further investigation into MREVI's practical applications in urban planning, climate regulation, carbon sink estimation, and environmental monitoring is essential to fully leverage its potential in supporting sustainable urban development.

CRediT authorship contribution statement

Ronghua Li: Writing – original draft, Visualization, Validation, Software, Methodology, Investigation, Formal analysis. **Shiping Ye:** Writing – review & editing, Writing – original draft, Validation, Supervision, Resources, Project administration, Methodology, Investigation,

Funding acquisition, Formal analysis, Conceptualization. **Zhican Bai:** Visualization, Validation, Methodology, Investigation, Formal analysis, Data curation. **Alexander Nedzved:** Validation, Supervision, Methodology, Formal analysis, Conceptualization. **Alexander Tuzikov:** Validation, Supervision, Methodology, Formal analysis, Conceptualization.

Declaration of competing interest

The authors declare that they have no known competing financial interests or personal relationships that could have appeared to influence the work reported in this paper.

Data availability

Data will be made available on request.

Acknowledgements

This research was funded by Ministry of Science and Technology of the People's Republic of China (Grant Number: G2023016002L).

References

Alavipanah, S. K., Karimi Firozjaei, M., Sedighi, A., Fathololoumi, S., Zare Naghadehi, S., Saleh, S., Naghdizadegan, M., Gomeh, Z., Arsanjani, J. J., Makki, M., Qureshi, S., Weng, Q., Haase, D., Pradgan, B., Biswas, A., M. Atkinson, P., 2022. The shadow effect on surface biophysical variables derived from remote sensing: a review. Land. 11(11), 2025. doi: 10.3390/land11112025.

Beale, J., Grabowski, R.C., Lokidor, P.L.O., Vercruysse, K., Simms, D.M., 2022. Vegetation cover dynamics along two Himalayan rivers: Drivers and implications of change. Sci. Total Environ. 849, 157826. https://doi.org/10.1016/j.scitotenv.2022.157826.

Behera, T.K., Bakshi, S., Sa, P.K., 2023. A lightweight deep learning architecture for vegetation segmentation using UAV-captured aerial images. Sust. Comput. 37, 100841. https://doi.org/10.1016/j.suscom.2022.100841.

Bendig, J., Yu, K., Aasen, H., Bolten, A., Bennertz, S., Broscheit, J., Gnyp, M.L., Bareth, G., 2015. Combining UAV-based plant height from crop surface models, visible, and near infrared vegetation indices for biomass monitoring in barley. Int. J. Appl. Earth Obs. 39, 79–87. https://doi.org/10.1016/j.jag.2015.02.012.

Bhandari, A.K., Kumar, A., Singh, G.K., 2012. Feature extraction using Normalized Difference Vegetation Index (NDVI): A case study of Jabalpur city. Procedia Technol. 6, 612–621. https://doi.org/10.1016/j.protcy.2012.10.074.

Bi, H., Chen, W., Yang, Y., 2024. Extracting illuminated vegetation, shadowed vegetation and background for finer fractional vegetation cover with polarization information and a convolutional network. Precis. Agric. 25 (2), 1106–1125. https://doi.org/10.1007/s11119-023-10094-w.

Braga, P., Crusiol, L.G.T., Nanni, M.R., Caranhato, A.L.H., Fuhrmann, M.B., Nepomuceno, A.L., Neumaier, N., Farias, J.R.B., Koltun, A., Gonçalves, L.S.A., Mertz-Henning, L.M., 2021. Vegetation indices and NIR-SWIR spectral bands as a phenotyping tool for water status determination in soybean. Precis. Agric. 22, 249–266. https://doi.org/10.1007/s11119-020-09740-4.

Candiago, S., Remondino, F., De Giglio, M., Dubbini, M., Gattelli, M., 2015. Evaluating multispectral images and vegetation indices for precision farming applications from UAV images. Remote Sens. 7 (4), 4026–4047. https://doi.org/10.3390/rs70404026.

Cao, S., Danielson, B., Clare, S., Koenig, S., Campos-Vargas, C., Sanchez-Azofeifa, A., 2019. Radiometric calibration assessments for UAS-borne multispectral cameras: Laboratory and field protocols. ISPRS J. Photogramm. Remote Sens. 149, 132–145. https://doi.org/10.1016/j.isprsjprs.2019.01.016.

Cao, Y., Li, Y., Shen, S., Wang, W., Peng, X., Chen, J., Liao, J., Lv, X., Liu, Y., Ma, L., Hu, G., Jiang, J., Sun, D., Jiang, Q., Liao, Q., 2024. Mapping urban green equity and analysing its impacted mechanisms: A novel approach. Sustain. Cities Soc. 101, 105071. https://doi.org/10.1016/j.scs.2023.105071.

Chen, W., Huang, H., Dong, J., Zhang, Y., Tian, Y., Yang, Z., 2018. Social functional mapping of urban green space using remote sensing and social sensing data. ISPRS J. Photogramm. Remote Sens. 146, 436–452. https://doi.org/10.1016/j.isprsjprs.2018.10.010.

Chen, S., Li, Z., Ji, T., Zhao, H., Jiang, X., Gao, X., Pan, J., Zhang, W., 2022. Two-stepwise hierarchical adaptive threshold method for automatic rapeseed mapping over Jiangsu using harmonized Landsat/Sentinel-2. Remote Sens. 14 (11), 2715. https://doi.org/10.3390/rs14112715.

Chen, B., Nie, Z., Chen, Z., Xu, B., 2017. Quantitative estimation of 21st-century urban greenspace changes in Chinese populous cities. Sci. Total Environ. 609, 956–965. https://doi.org/10.1016/j.scitotenv.2017.07.238.

Chen, C., Yuan, X., Gan, S., Luo, W., Bi, R., Li, R., Gao, S., 2024. A new vegetation index based on UAV for extracting plateau vegetation information. Int. J. Appl. Earth Obs. 128, 103668. https://doi.org/10.1016/j.jag.2024.103668.

Cheng, Y., Wang, W., Ren, Z., Zhao, Y., Liao, Y., Ge, Y., Wang, J., He, J., Gu, Y., Wang, Y., Zhang, W., Zhang, C., 2023. Multi-scale Feature Fusion and Transformer Network for urban green space segmentation from high-resolution remote sensing images. Int. J. Appl. Earth Obs. 124, 103514. https://doi.org/10.1016/j.jag.2023.103514.

Delavarpour, N., Koparan, C., Nowatzki, J., Bajwa, S., Sun, X., 2021. A technical study on UAV characteristics for precision agriculture applications and associated practical challenges. Remote Sens. 13 (6), 1204. https://doi.org/10.3390/rs13061204.

Delegido, J., Verrelst, J., Meza, C.M., Rivera, J.P., Alonso, L., Moreno, J., 2013. A red-edge spectral index for remote sensing estimation of green LAI over agroecosystems. Eur. J. Agron. 46, 42–52. https://doi.org/10.1016/j.eja.2012.12.001.

Deng, R., Yang, G., Wang, W., Li, Y., Zhang, X., Hu, F., Guo, Q., Jia, M., 2024. A new method of estimating shelterbelt carbon storage on the regional scale: Combined the single tree carbon storage with tree numbers. Ecol. Indic. 163, 112071. https://doi.org/10.1016/j.ecolind.2024.112071.

Di, S., Li, Z.L., Tang, R., Pan, X., Liu, H., Niu, Y., 2019. Urban green space classification and water consumption analysis with remote-sensing technology: a case study in Beijing. China. Int. J. Remote Sens. 40 (5–6), 1909–1929. https://doi.org/10.1080/01431161.2018.1479798.

Diener, A., Mudu, P., 2021. How can vegetation protect us from air pollution? A critical review on green spaces' mitigation abilities for air-borne particles from a public health perspective-with implications for urban planning. Sci. Total Environ. 796, 148605. https://doi.org/10.1016/j.scitotenv.2021.148605.

Dong, T., Liu, J., Shang, J., Qian, B., Ma, B., Kovacs, J.M., Walters, D., Jiao, X., Geng, X., Shi, Y., 2019. Assessment of red-edge vegetation indices for crop leaf area index estimation. Remote Sens. Environ. 222, 133–143. https://doi.org/10.1016/j.rse.2018.12.032.

Dong, L., Yu, G., Ogunbona, P., Li, W., 2008. An efficient iterative algorithm for image thresholding. Pattern Recognit. Lett. 29 (9), 1311–1316. https://doi.org/10.1016/j.patrec.2008.02.001.

Ercolani, G., Chiaradia, E.A., Gandolfi, C., Castelli, F., Masseroni, D., 2018. Evaluating performances of green roofs for stormwater runoff mitigation in a high flood risk urban catchment. J. Hydrol. 566, 830–845. https://doi.org/10.1016/j.jhydrol.2018.09.050.

Feng, Q., Liu, J., Gong, J., 2015. UAV remote sensing for urban vegetation mapping using random forest and texture analysis. Remote Sens. 7 (1), 1074–1094. https://doi.org/10.3390/rs70101074.

Filella, I., Penuelas, J. 1., 1994. The red edge position and shape as indicators of plant chlorophyll content, biomass and hydric status. Int. J. Remote Sens. 15(7), 1459-1470. doi: 10.1080/01431169408954177.

Fu, J., Fu, H., Zhu, C., Sun, Y., Cao, H., 2024. Assessing the health risk impacts of urban green spaces on air pollution-Evidence from 31 China's provinces. Ecol. Indic. 159, 111725. https://doi.org/10.1016/j.ecolind.2024.111725.

Gao, L., Wang, X., Johnson, B.A., Tian, Q., Wang, Y., Verrelst, J., Mu, X., Gu, X., 2020. Remote sensing algorithms for estimation of fractional vegetation cover using pure vegetation index values: A review. ISPRS J. Photogramm. Remote Sens. 159, 364–377. https://doi.org/10.1016/j.isprsjprs.2019.11.018.

Gitelson, A., Merzlyak, M.N., 1994. Spectral reflectance changes associated with autumn senescence of Aesculus hippocastanum L. and Acer platanoides L. leaves. Spectral features and relation to chlorophyll estimation. J. Plant Physiol., 143(3), 286-292. doi: 10.1016/S0176-1617(11)81633-0.

Gitelson, A.A., Kaufman, Y.J., Merzlyak, M.N., 1996. Use of a green channel in remote sensing of global vegetation from EOS-MODIS. Remote Sens. Environ. 58 (3), 289–298. https://doi.org/10.1016/S0034-4257(96)00072-7.

Guo, X., Wang, M., Jia, M., Wang, W., 2021a. Estimating mangrove leaf area index based on red-edge vegetation indices: A comparison among UAV, WorldView-2 and Sentinel-2 imagery. Int. J. Appl. Earth Obs. 103, 102493. https://doi.org/10.1016/j.jag.2021.102493.

Guo, Z.C., Wang, T., Liu, S.L., Kang, W.P., Chen, X., Feng, K., Zhang, X., Zhi, Y., 2021b. Biomass and vegetation coverage survey in the Mu Us sandy land-based on unmanned aerial vehicle RGB images. Int. J. Appl. Earth Obs. 94, 102239. https://doi.org/10.1016/j.jag.2020.102239.

Herold, M., Roberts, D.A., Gardner, M.E., Dennison, P.E., 2004. Spectrometry for urban area remote sensing—Development and analysis of a spectral library from 350 to 2400 nm. Remote Sens. Environ. 91 (3–4), 304–319. https://doi.org/10.1016/j.rse.2004.02.013.

Horler, D.N.H., Dockray, M., Barber, J., 1983. The red edge of plant leaf reflectance. Int. J. Remote Sens. 4 (2), 273–288. https://doi.org/10.1080/01431168308948546.

Hu, J., Niu, H., Carrasco, J., Lennox, B., Arvin, F., 2022. Fault-tolerant cooperative navigation of networked UAV swarms for forest fire monitoring. Aerosp. Sci. Technol. 123, 107494. https://doi.org/10.1016/j.ast.2022.107494.

Huang, S., Tang, L., Hupy, J.P., Wang, Y., Shao, G., 2021. A commentary review on the use of normalized difference vegetation index (NDVI) in the era of popular remote sensing. J. for. Res. 32 (1), 1–6. https://doi.org/10.1007/s11676-020-01155-1.

Huete, A., Didan, K., Miura, T., Rodriguez, E.P., Gao, X., Ferreira, L.G., 2002. Overview of the radiometric and biophysical performance of the MODIS vegetation indices. Remote Sens. Environ. 83 (1–2), 195–213. https://doi.org/10.1016/S0034-4257(02)00096-2.

Ibrahim, I., Samah, A.A., Fauzi, R., 2014. Biophysical factors of remote sensing approach in urban green analysis. Geocarto Int. 29 (7), 807–818. https://doi.org/10.1080/10106049.2013.859306.

Khodadad, M., Aguilar-Barajas, I., Khan, A.Z., 2023. Green infrastructure for urban flood resilience: a review of recent literature on bibliometrics, methodologies, and typologies. Water. 15 (3), 523. https://doi.org/10.3390/w15030523.

Kim, H.W., Park, Y., 2016. Urban green infrastructure and local flooding: The impact of landscape patterns on peak runoff in four Texas MSAs. Appl. Geogr. 77, 72–81. https://doi.org/10.1016/j.apgeog.2016.10.008.

Knipling, E.B., 1970. Physical and physiological basis for the reflectance of visible and near-infrared radiation from vegetation. Remote Sens. Environ. 1 (3), 155–159. https://doi.org/10.1016/S0034-4257(70)80021-9.
Kopecká, M., Szatmári, D., Rosina, K., 2017. Analysis of urban green spaces based on Sentinel-2A: Case studies from Slovakia. Land. 6 (2), 25. https://doi.org/10.3390/land6020025.
Lewińska, K.E., Hostert, P., Buchner, J., Bleyhl, B., Radeloff, V.C., 2020. Short-term vegetation loss versus decadal degradation of grasslands in the Caucasus based on Cumulative Endmember Fractions. Remote Sens. Environ. 248, 111969. https://doi.org/10.1016/j.rse.2020.111969.
Li, C., Peng, C., Chiang, P.C., Cai, Y., Wang, X., Yang, Z., 2019. Mechanisms and applications of green infrastructure practices for stormwater control: A review. J. Hydrol. 568, 626–637. https://doi.org/10.1016/j.jhydrol.2018.10.074.
Li, F., Zeng, Y., Luo, J., Ma, R., Wu, B., 2016. Modeling grassland aboveground biomass using a pure vegetation index. Ecol. Indic. 62, 279–288. https://doi.org/10.1016/j.ecolind.2015.11.005.
Liu, J., Fan, J., Yang, C., Xu, F., Zhang, X., 2022. Novel vegetation indices for estimating photosynthetic and non-photosynthetic fractional vegetation cover from Sentinel data. Int. J. Appl. Earth Obs. 109, 102793. https://doi.org/10.1016/j.jag.2022.102793.
Luo, S., Li, H., Shen, H., 2020. Deeply supervised convolutional neural network for shadow detection based on a novel aerial shadow imagery dataset. ISPRS J. Photogramm. Remote Sens. 167, 443–457. https://doi.org/10.1016/j.isprsjprs.2020.07.016.
Lyu, X., Li, X., Dang, D., Dou, H., Wang, K., Lou, A., 2022. Unmanned aerial vehicle (UAV) remote sensing in grassland ecosystem monitoring: A systematic review. Remote Sens. 14 (5), 1096. https://doi.org/10.3390/rs14051096.
Nero, B.F., 2017. Urban green space dynamics and socio-environmental inequity: Multi-resolution and spatiotemporal data analysis of Kumasi. Ghana. Int. J. Remote Sens. 38 (23), 6993–7020. https://doi.org/10.1080/01431161.2017.1370152.
Neyns, R., Canters, F., 2022. Mapping of urban vegetation with high-resolution remote sensing: A review. Remote Sens. 14 (4), 1031. https://doi.org/10.3390/rs14041031.
Pu, R., Landry, S., 2012. A comparative analysis of high spatial resolution IKONOS and WorldView-2 imagery for mapping urban tree species. Remote Sens. Environ. 124, 516–533. https://doi.org/10.1016/j.rse.2012.06.011.
Qi, T., Ren, Q., Zhang, D., Lu, W., He, C., 2023. Impacts of urban expansion on vegetation in drylands: A multiscale analysis based on the vegetation disturbance index. Ecol. Indic. 147, 109984. https://doi.org/10.1016/j.ecolind.2023.109984.
Qin, H., Zhou, W., Qian, Y., Zhang, H., Yao, Y., 2022. Estimating aboveground carbon stocks of urban trees by synergizing ICESat-2 LiDAR with GF-2 data. Urban for. Urban Green. 76, 127728. https://doi.org/10.1016/j.ufug.2022.127728.
Richards, D.R., Belcher, R.N., 2019. Global changes in urban vegetation cover. Remote Sens. 12 (1), 23. https://doi.org/10.3390/rs12010023.
Rokni, K., Musa, T.A., 2019. Normalized difference vegetation change index: A technique for detecting vegetation changes using Landsat imagery. Catena. 178, 59–63. https://doi.org/10.1016/j.catena.2019.03.007.
Rouse, J.W., Haas, R.H., Schell, J.A., Deering, D.W., 1974. Monitoring vegetation systems in the Great Plains with ERTS. NASA Spec. Publ. 351 (1), 309.
Sæbø, A., Popek, R., Nawrot, B., Hanslin, H.M., Gawronska, H., Gawronski, S.W., 2012. Plant species differences in particulate matter accumulation on leaf surfaces. Sci. Total Environ. 427, 347–354. https://doi.org/10.1016/j.scitotenv.2012.03.084.
Sathyakumar, V., Ramsankaran, R.A.A.J., Bardhan, R., 2019. Linking remotely sensed Urban Green Space (UGS) distribution patterns and Socio-Economic Status (SES)-A multi-scale probabilistic analysis based in Mumbai. India. Gisci. Remote Sens. 56 (5), 645–669. https://doi.org/10.1080/15481603.2018.1549819.
Sims, D.A., Gamon, J.A., 2002. Relationships between leaf pigment content and spectral reflectance across a wide range of species, leaf structures and developmental stages. Remote Sens. Environ. 81 (2–3), 337–354. https://doi.org/10.1016/S0034-4257(02)00010-X.
Song, Z., Lu, Y., Ding, Z., Sun, D., Jia, Y., Sun, W., 2023. A New Remote Sensing Desert Vegetation Detection Index. Remote Sens. 15 (24), 5742. https://doi.org/10.3390/rs15245742.
Song, B., Park, K., 2020. Detection of aquatic plants using multispectral UAV imagery and vegetation index. Remote Sens. 12 (3), 387. https://doi.org/10.3390/rs12030387.
Sotille, M.E., Bremer, U.F., Vieira, G., Velho, L.F., Petsch, C., Simões, J.C., 2020. Evaluation of UAV and satellite-derived NDVI to map maritime Antarctic vegetation. Appl. Geogr. 125, 102322. https://doi.org/10.1016/j.apgeog.2020.102322.
Staccione, A., Essenfelder, A.H., Bagli, S., Mysiak, J., 2024. Connected urban green spaces for pluvial flood risk reduction in the Metropolitan area of Milan. Sustain. Cities Soc. 104, 105288. https://doi.org/10.1016/j.scs.2024.105288.
Sun, G., Jiao, Z., Zhang, A., Li, F., Fu, H., Li, Z., 2021. Hyperspectral image-based vegetation index (HSVI): A new vegetation index for urban ecological research. Int. J. Appl. Earth Obs. 103, 102529. https://doi.org/10.1016/j.jag.2021.102529.
Tang, J., Luo, Q., Guo, F., Wu, Z., Xiao, X., Gao, Y., 2020. SDRNet: An end-to-end shadow detection and removal network. Signal Process. Image Commun. 84, 115832. https://doi.org/10.1016/j.image.2020.115832.
Timmer, B., Reshitnyk, L.Y., Hessing-Lewis, M., Juanes, F., Costa, M., 2022. Comparing the use of red-edge and near-infrared wavelength ranges for detecting submerged kelp canopy. Remote Sens. 14 (9), 2241. https://doi.org/10.3390/rs14092241.
Veraverbeke, S., Gitas, I., Katagis, T., Polychronaki, A., Somers, B., Goossens, R., 2012. Assessing post-fire vegetation recovery using red–near infrared vegetation indices: Accounting for background and vegetation variability. ISPRS J. Photogramm. Remote Sens. 68, 28–39. https://doi.org/10.1016/j.isprsjprs.2011.12.007.
Wang, T., Chandra, A., Jung, J., Chang, A., 2022a. UAV remote sensing based estimation of green cover during turfgrass establishment. Comput. Electron. Agric. 194, 106721. https://doi.org/10.1016/j.compag.2022.106721.
Wang, Z., Li, Z., Wang, Y., Zheng, X., Deng, X., 2024. Building green infrastructure for mitigating urban flood risk in Beijing. China. Urban for. Urban Green. 93, 128218. https://doi.org/10.1016/j.ufug.2024.128218.
Wang, W., Liu, R., Gan, F., Zhou, P., Zhang, X., Ding, L., 2021. Monitoring and evaluating restoration vegetation status in mine region using remote sensing data: Case study in Inner Mongolia. China. Remote Sens. 13 (7), 1350. https://doi.org/10.3390/rs13071350.
Wang, X., Lu, X., Li, G., Wang, J., Yang, Z., Zhou, Y., Feng, Z., 2022b. Combining the red edge-near infrared vegetation indexes of DEM to extract urban vegetation information. Spectrosc. Spect. Anal. 42 (7), 2284–2289. https://doi.org/10.3964/j.issn.1000-0593(2022)07-2284-06.
Wójcik-Długoborska, K.A., Bialik, R.J., 2020. The influence of shadow effects on the spectral characteristics of glacial meltwater. Remote Sens. 13 (1), 36. https://doi.org/10.3390/rs13010036.
Xu, Z., Liu, J., Yu, K., Liu, T., Gong, C., Tang, M., Xie, W., Li, Z., 2013. Construction of vegetation shadow index (SVI) and application effects in four remote sensing images. Spectrosc. Spect. Anal. 33 (12), 3359–3365. https://doi.org/10.3964/j.issn.1000-0593(2013)12-3359-07.
Xu, A., Wang, F., Li, L., 2023. Vegetation information extraction in karst area based on UAV remote sensing in visible light band. Optik. 272, 170355. https://doi.org/10.1016/j.ijleo.2022.170355.
Yan, G., Li, L., Coy, A., Mu, X., Chen, S., Xie, D., Zhang, W., Shen, Q., Zhou, H., 2019. Improving the estimation of fractional vegetation cover from UAV RGB imagery by colour unmixing. ISPRS J. Photogramm. Remote Sens. 158, 23–34. https://doi.org/10.1016/j.isprsjprs.2019.09.017.
Yang, J., Guan, Y., Xia, J.C., Jin, C., Li, X., 2018. Spatiotemporal variation characteristics of green space ecosystem service value at urban fringes: A case study on Ganjingzi District in Dalian. China. Sci. Total Environ. 639, 1453–1461. https://doi.org/10.1016/j.scitotenv.2018.05.253.
Yang, Z., Yu, X., Dedman, S., Rosso, M., Zhu, J., Yang, J., Xia, Y., Tian, Y., Zhang, G., Wang, J., 2022. UAV remote sensing applications in marine monitoring: Knowledge visualization and review. Sci. Total Environ. 838, 155939. https://doi.org/10.1016/j.scitotenv.2022.155939.
Yu, S., Yu, B., Song, W., Wu, B., Zhou, J., Huang, Y., Wu, J., Zhao, F., Mao, W., 2016. View-based greenery: A three-dimensional assessment of city buildings' green visibility using Floor Green View Index. Landsc. Urban Plan. 152, 13–26. https://doi.org/10.1016/j.landurbplan.2016.04.004.
Zahoor, A., Xu, T., Wang, M., Dawood, M., Afrane, S., Li, Y., Chen, J., Mao, G., 2023. Natural and artificial green infrastructure (GI) for sustainable resilient cities: a scientometric analysis. Environ. Impact Assess. Rev. 101, 107139. https://doi.org/10.1016/j.eiar.2023.107139.
Zhang, J., Qiu, X., Wu, Y., Zhu, Y., Cao, Q., Liu, X., Cao, W., 2021. Combining texture, color, and vegetation indices from fixed-wing UAS imagery to estimate wheat growth parameters using multivariate regression methods. Comput. Electron. Agric. 185, 106138. https://doi.org/10.1016/j.compag.2021.106138.
Zhang, L., Sun, X., Wu, T., Zhang, H., 2015. An analysis of shadow effects on spectral vegetation indexes using a ground-based imaging spectrometer. IEEE Geosci. Remote Sens. Lett. 12 (11), 2188–2192. https://doi.org/10.1109/LGRS.2015.2450218.
Zhang, X., Zhang, F., Qi, Y., Deng, L., Wang, X., Yang, S., 2019. New research methods for vegetation information extraction based on visible light remote sensing images from an unmanned aerial vehicle (UAV). Int. J. Appl. Earth Obs. 78, 215–226. https://doi.org/10.1016/j.jag.2019.01.001.
Zhao, D., Cai, J., Xu, Y., Liu, Y., Yao, M., 2023. Carbon sinks in urban public green spaces under carbon neutrality: A bibliometric analysis and systematic literature review. Urban for. Urban Green. 128037. https://doi.org/10.1016/j.ufug.2023.128037.
Zhou, J., Huang, Y., Yu, B., 2014. Mapping vegetation-covered urban surfaces using seeded region growing in visible-NIR air photos. IEEE J. Sel. Top. Appl. Earth Observ. Remote Sens. 8(5), 2212-2221. doi: 10.1109/JSTARS.2014.2362308.
Zhou, G., Ren, H., Liu, T., Zhou, L., Ji, Y., Song, X., Lv, X., 2023. A new regional vegetation mapping method based on terrain-climate-remote sensing and its application on the Qinghai-Xizang Plateau. Sci. China-Earth Sci. 66 (2), 237–246. https://doi.org/10.1007/s11430-022-1006-1.
Zhu, Y., Liu, K., Liu, L., Myint, S.W., Wang, S., Liu, H., He, Z., 2017. Exploring the potential of worldview-2 red-edge band-based vegetation indices for estimation of mangrove leaf area index with machine learning algorithms. Remote Sens. 9 (10), 1060. https://doi.org/10.3390/rs9101060.
Zhuang, Q., Shao, Z., Gong, J., Li, D., Huang, X., Zhang, Y., Xu, X., Dang, C., Chen, J., Altan, O., Wu, S., 2022. Modeling carbon storage in urban vegetation: Progress, challenges, and opportunities. Int. J. Appl. Earth Obs. 114, 103058. https://doi.org/10.1016/j.jag.2022.103058.